# Atomic Resolution Imaging of Gold Nanoparticle Generation and Growth in Ionic Liquids

Taro Uematsu,[†,‡] Masahiro Baba,[‡] Yoshifumi Oshima,[§] Tetsuya Tsuda,[‡] Tsukasa Torimoto,[∥] and Susumu Kuwabata*,[‡]

[†]Frontier Research Base for Global Young Researchers, Graduate School of Engineering, Osaka University, 2-1 Yamada-oka, Suita, Osaka 565-0871, Japan

[‡]Department of Applied Chemistry, Graduate School of Engineering, Osaka University, 2-1 Yamada-oka, Suita, Osaka 565-0871, Japan

[§]School of Materials Science, Japan Advanced Institute of Science and Technology, Nomi, Ishikawa 923-1292, Japan

[∥]Department of Crystalline Materials Science, Graduate School of Engineering, Nagoya University, Chikusa-ku, Nagoya 464-8603, Japan

**S** *Supporting Information*

**ABSTRACT:** Recent advances in in situ transmission electron microscopy (TEM) techniques have provided unprecedented knowledge of chemical reactions from a microscopic viewpoint. To introduce volatile liquids, in which chemical reactions take place, use of sophisticated tailor-made fluid cells is a usual method. Herein, a very simple method is presented, which takes advantage of nonvolatile ionic liquids without any fluid cell. This method is successfully employed to investigate the essential steps in the generation of gold nanoparticles as well as the growth kinetics of individual particles. The ionic liquids that we select do not exhibit any anomalous effects on the reaction process as compared with recent in situ TEM studies using conventional solvents. Thus, obtained TEM movies largely support not only classical theory of nanoparticle generation but also some nonconventional phenomena that have been expected recently by some researchers. More noteworthy is the clear observation of lattice fringes by high-resolution TEM even in the ionic liquid media, providing intriguing information correlating coalescence with crystal states. The relaxation of nanoparticle shape and crystal structure after the coalescence is investigated in detail. The effect of crystal orientation upon coalescence is also analyzed and discussed.
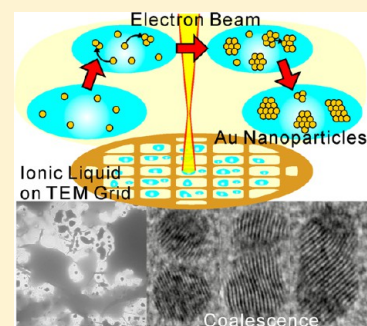
## INTRODUCTION

With growing interest in nanomaterials as catalysts, phosphors, and building blocks for complicated nanostructures, the synthesis of colloidal nanoparticles has been of central interest.[1−3] The size, shape, and monodispersity of nanoparticles as ensembles decide their optical, electronic, and catalytic properties. Therefore, scientists have investigated the synthesis of highly monodispersed, well-shape-controlled nanoparticles.[4−7] As such, researchers are actively engaged in comprehending the complex processes by which nanoparticles are generated.

As described by classical theory, nanoparticle generation includes nucleation and growth processes,[8−10] where reductively formed gold monomers, for example, nucleate to form clusters made of a fixed number of gold atoms during the first stage of the reaction, and the clusters continue to grow by the diffusion-driven deposition of gold monomers to existing nanoparticles,[7] as depicted in Figure 1. Ostwald ripening is known as another coarsening mechanism driven by the higher solubility of small nanoparticles,[11,12] which is given as $C_r$ with respect to the bulk solubility $C_\infty$ in the Gibbs−Thomson equation as
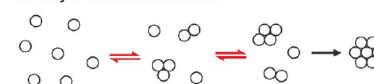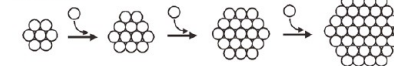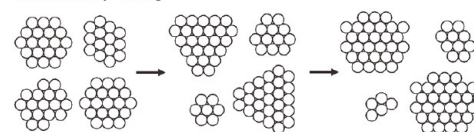


**Figure 1.** Classical model for nanoparticle generation, including nucleation, growth, and Ostwald ripening.

$$C_r = C_\infty \exp\left(\frac{2\gamma v}{kTr}\right)$$

(1)

where $\gamma$, $\nu$, $k$, $T$, and $r$ are the surface tension of a nanoparticle liquid interface, the atomic volume of components, Boltzmann's constant, temperature, and the particle radius, respectively. On the other hand, coalescence between particles, which is also known as aggregative growth, has recently been revealed to play a significant role in the growth of nanoparticles.[13,14] Some in situ techniques, such as X-ray absorption fine structure, small-angle X-ray scattering,[14] and optical spectroscopy for semiconductor nanoparticles[15−17] have been demonstrated to clarify such complicated and controversial mechanisms.

In situ transmission electron microscope (TEM) has another advantage to the aforementioned techniques, which is the traceability of individual particles rather than recording signals from an ensemble.[18] The first in situ TEM observation with a fluid cell was reported by Williamson et al. for the electrodeposition of copper nanoparticles using silicon nitride windows to maintain an aqueous solution in a high-vacuum TEM chamber.[19] A later work by Zheng et al. in investigating free-standing Pt nanoparticle formation visualized for the first time nanoparticle growth relating to its motion in liquids.[20] Within a couple of years, Li et al. observed the coalescence process of iron oxide crystals on the scale of tens of nanometers at an atomic resolution.[21] However, making rigid fluid cells to seal off volatile liquids in a high-vacuum TEM chamber ($\sim10^{-5}$ Pa) while maintaining electron transparency is very difficult for nonspecialists. More recently, Yuk et al. provided a major improvement by using two sheets of graphene as a capsule to enclose volatile solutions.[22] The use of graphene monolayers has greatly improved resolution by reducing electron scattering to the extent that crystallographic studies of nanocrystals smaller than 5 nm are possible.

There is another possible method to realize a very simple in situ observation in TEM, which is the use of nonvolatile ionic liquids. For instance, some investigations on lithium ion batteries used ionic liquid mixtures as lithium sources upon the lithiation of electrodes.[23−28] The use of ionic liquids can save the fabrication of complicated fluid cells, or realize more efficient lithium ion supply being compared to the cells including solid/solid junction with solid electrolytes. All of these studies look at the electrode materials that are not fully covered with ionic liquids. However, in situ observation through ionic liquid membrane should be possible when the thickness is properly reduced. As a matter of fact, we have confirmed its possibility through in situ observation of electrochemical reactions in ionic liquids with a scanning electron microscope (SEM)[29,30] and TEM observation of metal nanoparticles dispersed in ionic liquid that were prepared by the metal sputtering onto ionic liquids.[31,32]

In this study, we propose a very simple method to realize the in situ TEM observation of nanoparticle formation, in which no specialized apparatus is needed. Nonvolatile property of ionic liquids afford the introduction to vacuum systems, not only to rough vacuum systems like a sputtering equipment but also a high-vacuum X-ray photoelectron spectrometer without any specific sealing arrangements.[33−36] In terms of nanoparticle formation, our recent investigations revealed that metal deposits are formed on the surface of ionic liquids containing metal salts during the scanning electron microscopy observation of them.[37,38] Moreover, radiation irradiation to a certain type of ionic liquid yielded metal nanoparticles inside the liquids by the partial radiolysis followed by the reduction reaction.[39,40] These results indicated that the choice of

appropriate ionic liquids that produce radicals lead to the nanoparticle generation inside the liquid in a similar manner as the chlorobenzene/oleylamine mixed solvent that was employed in the recent experiments by Zheng et al. and Yuk et al. Plus, it is reported that ionic liquids stabilize nanoparticles without adding a surface ligand and by means of some interaction with metals that is peculiar to their components.[41,42] These situations provided motivation to use ionic liquids in this study on in situ observation for nanoparticle generation.

## ■ RESULTS AND DISCUSSION

**TEM Observation of Ionic Liquid Droplets.** As will be mentioned in the Experimental Section, we loaded ionic liquids diluted with ethanol on a TEM grid mesh and then dried. Thus, numerous ionic liquid droplets of various sizes were confirmed by TEM with low magnification as shown in Figure 2. They were stably observed without any evidence of
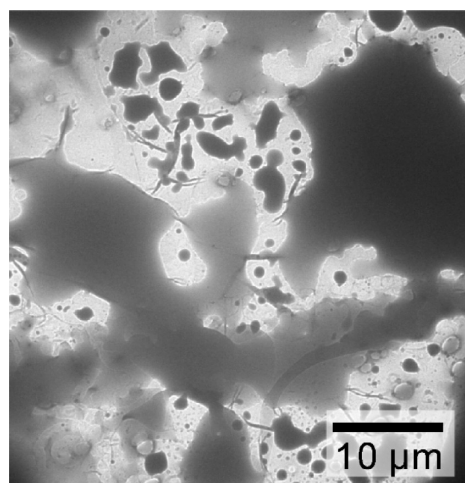


**Figure 2.** Low-magnification TEM image of ionic liquid [N$_{3,1,1,1}$]-[Tf$_2$N] supported with a polymer/carbon membrane on a gold grid mesh.

drying. For the observation of nanoparticle generation, NaAuCl$_4$ was employed as a source material and dissolved in the ionic liquid. Since any matrices cause the electron scattering that must lower the contrast and spatial resolution inside the droplet, it is important to select one droplet that has an appropriate thickness giving moderate contrast. Among the various-sized nearly flat droplets, those having a transmittance of ca. 60% were found to be appropriate for the in situ observation.

**Thickness of Appropriate Ionic Liquid Droplet.** To know the dimension of droplets giving a transmittance of ca. 60% in which nanoparticles are generated, the thickness was calculated from the scattering contrast.[43] The probability of electrons scattered to the angle higher than $\alpha_0$ to be intercepted by an aperture is given by

$$\sigma_{el}(\alpha_0) = \frac{Z^2 R^2 \lambda^2 (1 + E/E_0)^2}{\pi a_H^2} \frac{1}{1 + (\alpha_0/\theta_0)^2} \qquad (2)$$

where $Z$, $\lambda$, and $a_H$ are the atomic number, de Broglie wavelength, and Bohr radius, respectively. $R$ is the screening radius given as $R = a_H z^{-1/3}$. The term $1 + E/E_0$ represents the relativistic increase in the mass of the accelerated electrons,

which is equal to $m/m_0$, in which the rest energy $E_0$ is given as $E_0 = m_0 c^2 = 511$ keV. $\theta_0$ is the characteristic angle given as $\theta_0 = \lambda/2\pi R$. Similarly, the probability for inelastic term can be written as

$$\sigma_{\text{inel}}(\alpha_0) = \frac{4ZR^2\lambda^2(1 + E/E_0)^2}{\pi a_H^2} \left\{ -\frac{1}{4[1 + (\alpha_0/\theta_0)^2]} + \ln\sqrt{1 + (1 + (\theta_0/\alpha_0)^2)} \right\} \tag{3}$$

Therefore, by using the number of atoms per gram, given as $N = N_A/A$, where $N_A$ and $A$ denotes Avogadro's number and the effective atomic mass, respectively, the scattering event can be described by the Lambert−Beer law given as

$$\frac{dn}{n} = -\frac{N_A}{A}[\sigma_{\text{el}}(\alpha_0) + \sigma_{\text{inel}}(\alpha_0)]dx \tag{4}$$

where $x$ is the mass thickness given as $x = \rho t$ using the density of the specimen $\rho$ and the geometric thickness $t$, and where $n$ is the number of unscattered electrons. Integration of eq 4 gives the transparency when an objective aperture having an angle $\alpha_0$ is used

$$T(\alpha_0) = n/n_0 = \exp[-x/x_k(\alpha_0)] = \exp[-\rho t/x_k(\alpha_0)] \tag{5}$$

where the contrast thickness $x_k(\alpha_0)$ is given by

$$\frac{1}{x_k(\alpha_0)} = \frac{4}{Z} \frac{\pi A a_H^2}{N_A Z^2 R^2 \lambda^2 (1 + E/E_0)^2} \left\{ \frac{Z - 1}{4[1 + (\alpha_0/\theta_0)^2]} + \ln\sqrt{1 + (\theta_0/\alpha_0)^2} \right\} \tag{6}$$

The effective atomic number $Z$ for molecules can be calculated from the following equation[44,45]

$$Z = \frac{\sum f_n Z_n^{1.3}}{f_n Z_n^{0.3}} \tag{7}$$

where $f_n$ is the atomic fraction of the element n in the material whose atomic number is $Z_n$. The effective atomic mass $A$ is given by

$$A = \frac{\sum f_n A_n}{\sum f_n} \tag{8}$$

where $A_n$ denotes the atomic mass of the element n.

The effective atomic number and atomic mass were calculated for the 1:1 (volume ratio) mixture of 1-butyl-3-methylimidazolium bis(trifluoromethylsulfonyl)amide ($[\text{C}_4\text{mim}][\text{Tf}_2\text{N}]$) and trimethylpropylammonium bis(trifluoromethylsulfonyl)amide ($[\text{N}_{3,1,1,1}][\text{Tf}_2\text{N}]$) and listed in Table 1, although the mixing ratio will be rationalized below. For the calculation, one ion pair of $[\text{C}_4\text{mim}][\text{Tf}_2\text{N}]$ and 1.1 ion pairs of $[\text{N}_{3,1,1,1}][\text{Tf}_2\text{N}]$ was considered to be a calculation unit according to the molecular ratio between the two types of ionic liquids. Then, an ionic liquid droplet having a transmittance of 0.626, in a typical case, is calculated and listed in Table 2. In this case, the thickness of the droplet was estimated to be approximately 80 nm. This value is much smaller than the liquid thickness of 200−400 nm in cases where the liquid cells composed of silicon nitride windows and separators are used.[20,21] The possibility to select a place having

**Table 1. Effective Atomic Numbers for the Mixture of $[\text{C}_4\text{mim}][\text{Tf}_2\text{N}]$ and $[\text{N}_{3,1,1,1}][\text{Tf}_2\text{N}]$**

|  | $[\text{C}_4\text{mim}][\text{Tf}_2\text{N}]$ | $[\text{N}_{3,1,1,1}][\text{Tf}_2\text{N}]$ | 1:1 (vol)[a] mixture[b] |
|---|---|---|---|
| C | 10 | 8 | 18.8 |
| H | 15 | 16 | 32.6 |
| F | 6 | 6 | 12.6 |
| N | 3 | 2 | 5.2 |
| O | 4 | 4 | 8.4 |
| S | 2 | 2 | 4.2 |
| $F_w$ | 419.4 | 382.3 | 840 |
| effective $Z$ | − | − | 6.381 |
| effective $A$ | − | − | 10.27 |

[a]Molecular ratio for $[\text{C}_4\text{mim}][\text{Tf}_2\text{N}]$:$[\text{N}_{3,1,1,1}][\text{Tf}_2\text{N}]$ is calculated to be 1:1.1. [b]Calculation unit contains 1 ion pair of $[\text{C}_4\text{mim}][\text{Tf}_2\text{N}]$ and 1.1 ion pairs of $[\text{N}_{3,1,1,1}][\text{Tf}_2\text{N}]$.

**Table 2. Parameters Used for Estimating the Ionic Liquid Thickness Giving a Transmittance ($T$) of 0.626**

| | |
|---|---|
| $T$ | 0.626 |
| $R$ (m) | $2.464 \times 10^{-11}$ |
| $a_H$ (m) | $5.30 \times 10^{-11}$ |
| $Z$ | 6.381 |
| $A$ (g mol$^{-1}$) | 10.27 |
| $E$ (keV) | 100 |
| $E_0$ (keV) | 551 |
| $\lambda$ (m) | $3.70 \times 10^{-12}$ |
| $\theta_0$ (rad) | 0.0239 |
| $\alpha$ (rad) | 0.0130 |
| $\rho$ (g m$^{-1}$) | $1.432 \times 10^6$ |
| thickness (nm) | 77.7 |

an appropriate liquid thickness is one of the advantages of the present in situ TEM observation method using nonvolatile ionic liquids. In addition, the lack of the need for any window materials is also advantageous to obtain higher resolution in TEM.

**Type of Ionic Liquids.** The use of $[\text{C}_4\text{mim}][\text{Tf}_2\text{N}]$, which is one of the common ionic liquids, resulted in the instant formation of gold nanoparticles that was too rapid to be tracked on video. Since observation requires a certain range of brightness, control over the reaction rate by the beam current is limited. One of the key techniques for the successful observation of nanoparticle generation is the use of the ionic liquid mixture that enables nanoparticles formation in a moderate duration. On the basis of the previous results suggesting that imidazolium-type ionic liquids are susceptible to the electron beam, while ammonium-type ionic liquids are stable against ionization,[39,40,46,47] several experiments were conducted prior to the primary investigation. As a result, a volume ratio of $[\text{C}_4\text{mim}][\text{Tf}_2\text{N}]$:$[\text{N}_{3,1,1,1}][\text{Tf}_2\text{N}]$ = 50:50 was found to be appropriate under a beam current density of 1−2 $\times 10^3$ Am$^{-2}$, spending several hours for the generation and growth of gold nanoparticles.

**Generation of Gold Nanoparticles in TEM.** Figure 3A shows TEM images of nanoparticle generation during the observation of a liquid membrane containing 100 mM NaAuCl$_4$. The corresponding video image is also provided as Supporting Information (Movie S1). A liquid membrane of uniform brightness demonstrated some sort of a separation process at 160 min, which is observable as a contrast in the TEM image. It is probable that heavy gold atoms aggregated because of the low solubility of the reduced species. At around
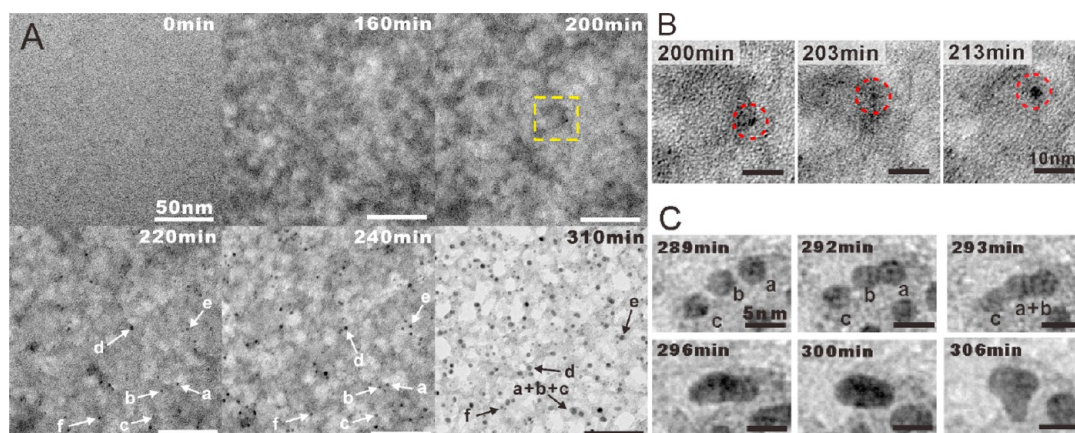
**Figure 3.** (A) 100 kV TEM images of Au nanoparticles generation and growth at 0, 160, 200, 220, 240, and 310 min after the initiation of electron beam irradiation. The specific particles temporally tracked in Figure 5 are labeled (a–f). (B) Magnified images of the area depicted in the yellow square in (A) showing the early stages of nucleation. (C) Successive coalescence of three nanoparticles (a–c) at around 290 min and the subsequent relaxation process.

200 min, very small black spots, which may be clusters composed of several tens of gold atoms, appeared from the relatively dark regions. The area surrounded by the yellow square was magnified and displayed in Figure 3B with two other images of the same area at different reaction times (203 and 213 min). Interestingly, the observed clusters did not undergo continuous growth but rather repeatedly increased and decreased their sizes until growth attained a particular level. These observations resemble the classical model for nucleation, where embryos fluctuate their sizes over time until they attain a critical radius at which the free energy of the entire particle, given as the sum of crystal energy and surface energy, obtains a maximum value. Although there are still debates on the critical radius, for example, how small it is,[48] or whether the macroscopic classical model can be applied to the nanocluster system or not,[49] the present method provided some useful information. In our observations, most of the nanoparticles exhibited continuous growth, as predicted by the classical model, after about 230 min.

However, unlike the classical growth model that predicts monomer attachment to the growing nanoparticles, many small particles or clusters seemed to participate in growth. Concurrently with the observed classical growth, nanoparticles also swelled by absorbing small clusters that were sufficiently large to be visible by the TEM. The aggregative growth mechanism, which has been recently recognized by some researchers, definitely has a large influence on the coarsening of nanoparticles.[13] At the end of the reaction, coalescence between large particles, as shown in Figure 3C, occurred frequently, as is consistent with preceding reports.[20–22]

A slow but continuous brightness change that indicated the decrease in the ionic liquid thickness was seen during the long time irradiation. This phenomenon seemed to be caused by the displacement of the ionic liquid from the beam center to the periphery due to the momentum transfer from the electron beam[50] because a ring-shaped ionic liquid deposit at the periphery of the electron beam was often observed. However, such a direct effect by the electron beam to the nanoparticles seemed to be negligible, as judged by the basically random movements of each nanoparticle described below.

**Diffusion of Nanoparticles in Ionic Liquids.** During the whole growth processes, all nanoparticles moved randomly by the self-diffusion. The diffusion coefficient of nanoparticles ($D$) can be determined from TEM images of two-dimensional projection as[51]

$$D = \frac{\langle r_{\text{TEM}}^2 \rangle}{4t} \tag{9}$$

where $\langle r_{\text{TEM}}^2 \rangle$ is the mean-square displacement of particles in the TEM images during the time $t$. Diffusion coefficient derived by eq 9 was 0.01–0.1 nm$^2$s$^{-1}$, which is much slower than the theoretical value (ca. $1 \times 10^6$ nm$^2$ s$^{-1}$) calculated from the Stokes−Einstein equation $D = kT/6\pi\eta a$ with the radius $a = 2$ nm, $\eta = 60$ mPa s. However, such unexpectedly slow diffusion has also been reported in some pioneering studies involving normal solvents in thin, enclosed liquid reactors. For example, Yuk et al., who used $o$-dichlorobenzene as a main solvent reported a diffusion coefficient of 0.1−1.2 nm$^2$ s$^{-1}$ for Pt nanoparticles ranging from 0.28 to 0.55 nm in radius.[22] Even diffusion in conventional solvents, such as water and other organic solvents, has been reported to be much slower when they are spatially confined than when in a bulk state. Liao et al. concluded that the interaction of nanoparticles with substrates causes such slow diffusion.[52] In addition, the complicated local structure and altered relaxation process of spatially confined liquids are responsible for the phenomenon.[51] Ionic liquids reportedly have obvious nanostructures at interfaces with air, water, and metal, which are detectable by several surface-specific analysis techniques such as X-ray reflectivity, sum-frequency generation, and probe microscopy.[53−56] These interfaces also have particular dielectric and structural relaxation behavior that deviate from conventional models.[57−60] However, the diffusion rate of nanoparticles in ionic liquids determined in this study was comparable to that observed for normal, spatially confined solvents. At least with respect to particle motion, the effect of the local structure peculiar to ionic liquids seemed to be negligible; that is, we can treat them as nonvolatile "solvents" for in situ TEM observation.

**Growth Kinetics and Coalescence.** Quantitative information corresponding to Figure 3A (and Movie S1, Supporting Information) was collected and displayed in Figure 4 and Figure 5. Figure 4A shows the time course variation of the mean particle diameter and number density of particles. The first nucleation occurred between 200 and 230 min,
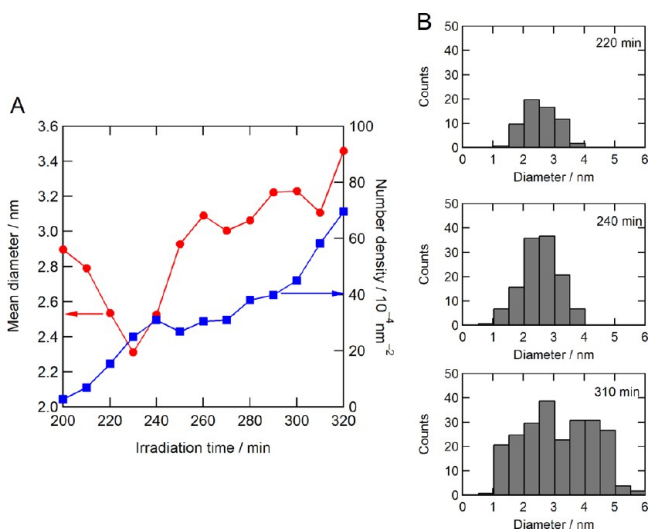
**Figure 4.** (A) Time-course variation of the mean diameter and number density of particles collected from the 100 kV TEM images shown in Figure 3A. (B) Histograms of particle size distribution at 220, 240, and 310 min.

during which the number of nanoparticles rapidly increased with a corresponding decrease in the average size. The first stage of nucleation ended at around 240 min, followed by particle growth by both monomer attachment and the aggregation of very small clusters. During this period, the number of nanoparticles stopped increasing or slightly decreased owing to aggregative growth, leading to the decrease in monomer consumption rate. Since the reduction of $AuCl_4^-$ occurred at a uniform rate, the accumulating Au monomers oversaturated, and finally, the second nucleation occurred from 270 min onward. Over the period of observation, the concentration of Au monomers remained high, as evidenced by multiple nucleation. The histograms of the resulting nanoparticle ensembles at 310 min (Figure 4B) separated into two major peaks, clearly representing the fact that two separate sets of nucleation occur at different reaction times, a phenomenon that should be avoided for obtaining mono-dispersed nanoparticle ensembles.

Time variations in diameters (Figure 5A) and volumes (Figure 5B) are displayed for the individual particles observed. Particles **a** through **e** spent the majority of time engaged in continuous growth. The increment of volume versus time was constant except for occasional jumps owing to coalescence, implying that diffusion-controlled monomer attachment was the dominant process for these particles. At 295 min, particles **a**, **b**, and **c** were subjected to coalescence, which is reflected as a jump in diameter for particle **a** and the termination of the plots for particles **b** and **c**. Sequential images obtained over the course of coalescence are displayed in Figure 3C, where the successive coalescence of the three nanoparticles and the following shape change to minimize the surface energy of the newly formed nanoparticle are included. As an exception, particle **f** stopped growing after 240 min and even slightly shrank after 270 min. During this period, particle **f** was surrounded by larger nanoparticles, as shown in Figure 3A at 310 min. This suggests that, in such a situation, the surrounding nanoparticles accumulated a large part of the available monomers due to their lower chemical potential. Thus, the growth of the smaller nanoparticle having a higher chemical potential ceased, indicating the importance of the
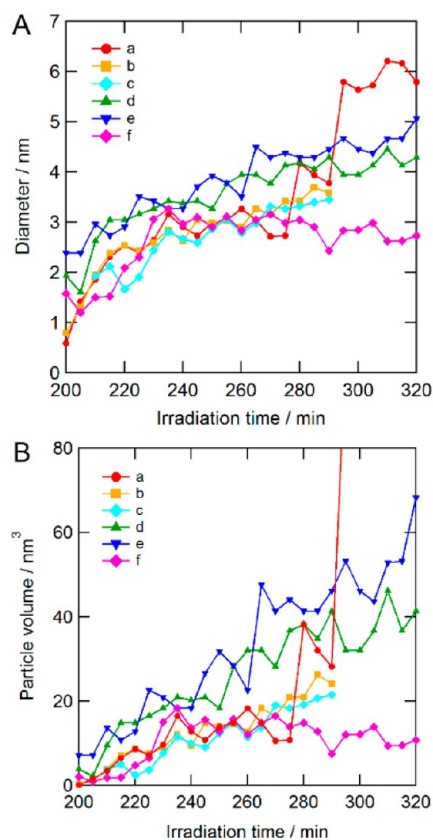


**Figure 5.** (A) Growth kinetics in diameter of the five Au nanoparticles labeled in Figure 3A. (B) The correponding volume calculated by $4/3\pi r^3$ from the radius $r$, which is estimated as the square root of the elliptical area divided by $\pi$.

local environment for the growth rate and the resulting monodispersity of nanoparticles. This situation is perhaps similar to Ostwald ripening. Obvious evidence for Ostwald ripening has been obtained in the high-resolution TEM (HRTEM) study that will be subsequently discussed.

**High-Resolution TEM Observation.** An HRTEM operated with a 300 kV acceleration voltage was used for further investigation of the initial nucleation processes and for the crystallographic analyses. Figure 6 shows various screen shots obtained from a video image (Supporting Information, Movie S2) recorded during the nanoparticle generation by electron beam irradiation in HRTEM. The corresponding variation of the mean volume and the number density of particles were collected and displayed in Figure 7A and 7B. Because of the 3 orders of magnitude larger current density used with HRTEM ($3-8 \times 10^6$ $Am^{2-}$), the latency time prior to nucleation became much shorter (120 s, Figure 7A) relative to observation by the 100 kV TEM (200 min, Figure 3A and 4A). The number density of particles was ca. 3 times higher, and its time variation reversed at 340 s in contrast to the nearly monotonic increase observed in the 100 kV TEM observation. During this period of decrement, the frequent coalescence and sudden disappearance of small nanoparticles were observed. Growth rates for individual nanoparticles are displayed in Figure 7B, the locations of which are represented in Figure 6. Particles **g** and **i**, and particles **h** and **j**, respectively, coalesced at 340 s, resulting in jumps in the volumes of particles **g** and **h**.
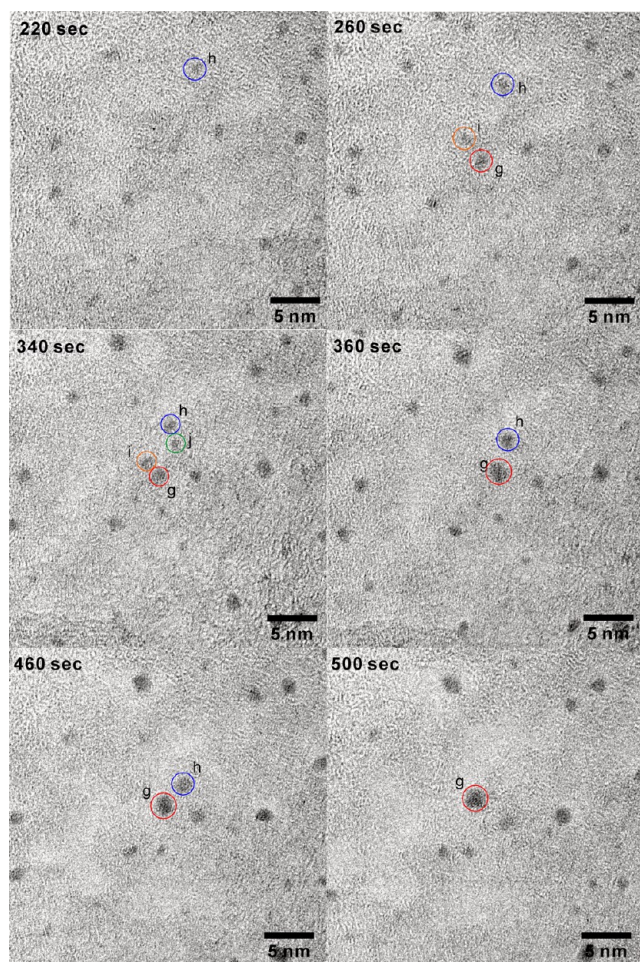
**Figure 6.** Sequential images of nanoparticle growth observed by HRTEM at different irradiation times. The volumes of the particles labeled as **g** through **j** in the images are tracked as a function of time in Figure 7B.



**Figure 7.** (A) Time-course variation of the mean particle volume and number density of particles during irradiation by electron beam in HRTEM. (B) Volume variations of the four selected nanoparticles labeled in Figure 6. (C) Sequential images during the disappearance of particle **h** owing to the process of Ostwald ripening.

Although the growth of particle **h** reversed, and eventually, the particle disappeared at 480 s, this phenomenon was different from simple coalescence. The overall process of disappearance is shown in the sequential images around particles **g** and **h** in Figure 7C and the magnified video image (Supporting Information, Movie S3). Particle **h**, initially located in the vicinity of particle **g**, suddenly began to shrink at 470 s. The apparent gap between the two particles ruled out the possibility of coalescence. Also, the observed swelling of the particle **g** (1.4 nm$^3$) was less than the last volume of particle **h** (2.2 nm$^3$), indicating that at least part of the components of **h** are not absorbed by **g**. These observations correspond with the phenomenon of Ostwald ripening, in which smaller particles of higher chemical potential are prone to dissolve to feed larger particles of lower chemical potential. The relatively small nanoparticle **h** therefore dissolved when it approached the larger particle **g**. A similar phenomenon was frequently observed in other regions during the same period.

**Atomic Resolution Imaging of Coalescence Processes.** Coalescence processes were also observed by HRTEM, which provided a resolution sufficiently high to obtain crystallographic information. Figure 8A shows sequential HRTEM images of nanoparticles during coalescence. The corresponding video is provided as Supporting Information (Movie S4). Two nanoparticles, a 3-fold twinned crystal **I** and
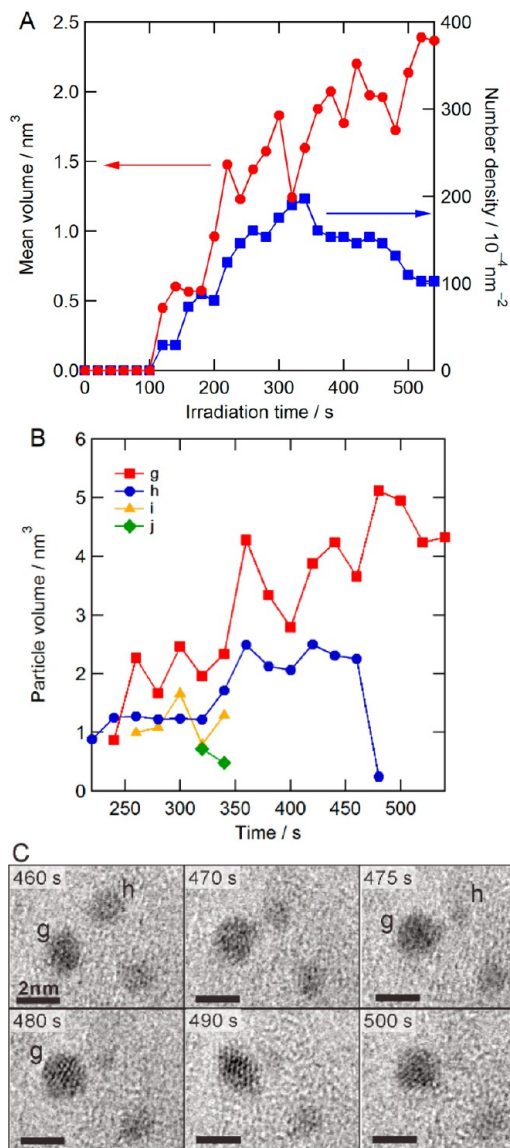
a single crystal **II**, were located in close vicinity at 0.0 s. Because of the small scattering angle of the accelerated electrons, the lattice fringes in TEM are only visible when the plane that one intends to view is directed parallel to the electron beam, typically within an accuracy of ±1°. During the first 23.9 s, particle **II** rotated to hide its (111) plane, and alternatively, the (200) plane became visible. In a short period, a new plane was generated between the two particles, the lattice space of which ranged between the (111) and (200) planes, as depicted in the fast Fourier transform images obtained at 27.1 and 30.3 s reaction times. This new phase bent rightward to fuse with the (111) plane of particle **I** at 31.9 s, followed by the rotation of the entire particle along its long axis until it showed the (111) plane at 36.1 s. After that, the particle started to change its shape to minimize its surface energy (52.7 and 88.6 s). The resulting nanoparticle recorded at 136.1 s in Figure 8B had the (111) twin plane, as illustrated
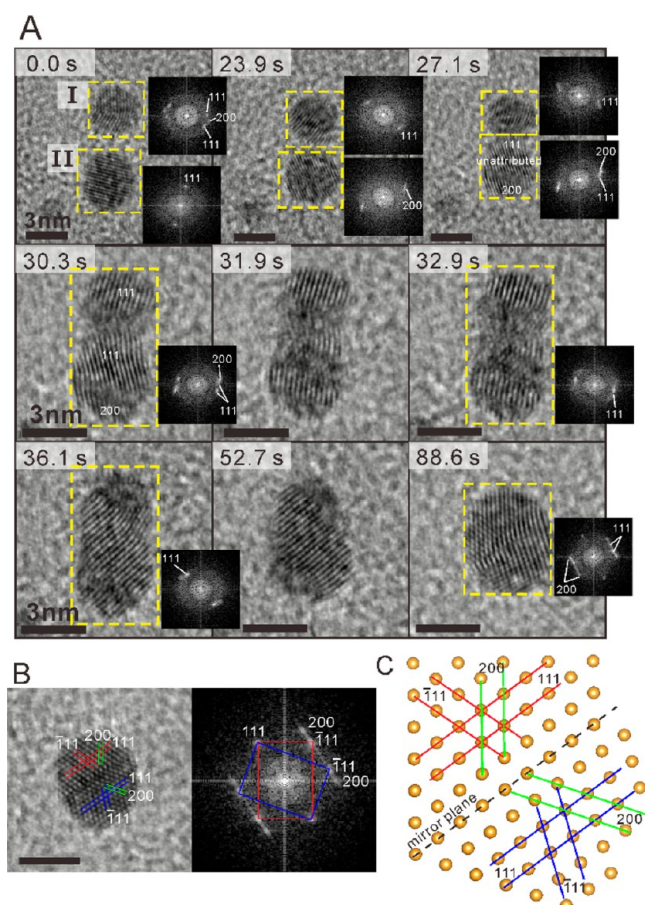
13794

dx.doi.org/10.1021/ja506724w | J. Am. Chem. Soc. 2014, 136, 13789–13797

**Figure 8.** (A) HRTEM images of two Au nanoparticles during the fusion process extracted from the movie Movie S4 (Supporting Information). The insets are fast Fourier transform of the selected areas depicted as yellow rectangles in the corresponding images. Scale bars in the images are all 3 nm. (B) Final structure (136.1 s) of the coalesced Au nanoparticles with its FFT image. (C) Schematic illustration of the crystal showing the (111) twin plane.



**Figure 9.** Images taken prior to (A1, B1, and C1) and during coalescence (A2, B2, and C2). Facets are displayed in the figures with broken lines, and indices are given in braces whenever possible.

in Figure 8C. Judging from the volume ratio of the two crystals in the twin, this boundary seemed to be formed by coalescence. On the other hand, the other two boundaries originating from the 3-fold twinned crystal I seemed to disappear during relaxation.

Through the observation of multiple sets of coalescence events, it was elucidated that coalescence requires some specific crystal orientations. Figure 9 shows three sets of TEM images before (A1, B1, C1) and shortly after coalescence (A2, B2, C2). Videos are provided as Movie S5, Movie S6, and Movie S7 (Supporting Information) for Figure 9A1−A2, B1−B2, and C1−C2, respectively. Facets are displayed with dotted lines and the indices with braces in all figures wherever possible. A notable difference between the three coalescence events is the latency time before the two particles initiate coalescence. For the top case (Figure 9A1 and A2), the approach velocity of the particles rapidly increased as their interval decreased, as if acted upon by some effective force. The two particles faced one another with unattributable facets (possibly {011}, {311}, or curving disordered planes), and there seemed to be no hindrance to the fusion of the two particles. On the other hand, for the middle case of facing {111} facets (Figure 9B1 and B2), the two nanoparticles paused for 20 min while maintaining a distance of 1.2 nm
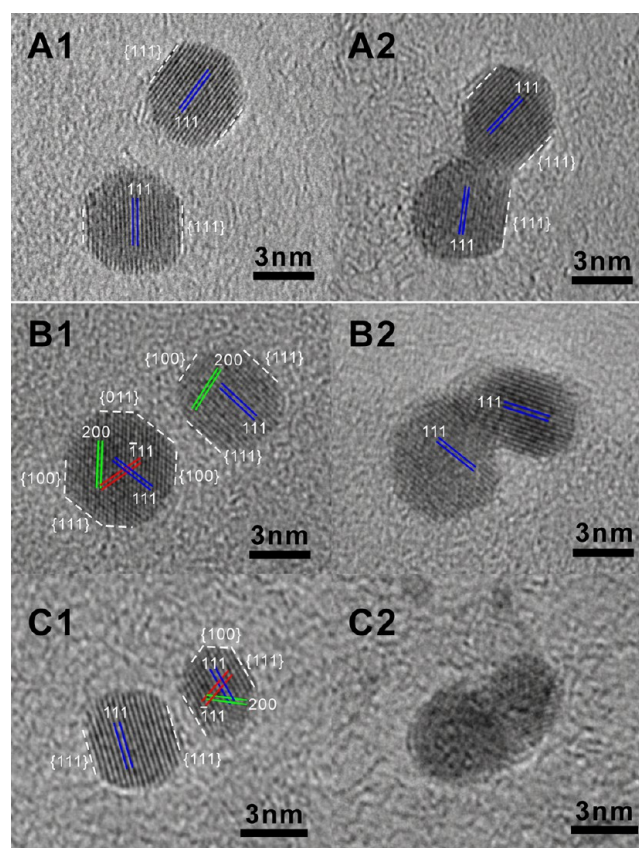
(Figure 9B1). The two particles finally coalesced with a curiously bended conformation as if to avoid contact between the {111} facets (Figure 9B2). For the bottom case (Figure 9C1 and C2), the particles also paused for 2 min while maintaining a 0.7 nm distance and then coalesced by the random rotation of both particles, which made it impossible to trace the crystal orientation. On the whole, in the coalescence series observations it was clearly observed that the {111} or {100} facets managed to inhibit coalescence. These facets are well-known as low-energy surfaces for the Au crystal;[61] that is, the significance of the surface energy of each facet was clearly demonstrated. Still, it is interesting to consider how the particles might possibly respond to their facets beyond a gap as large as 1 nm.

Structural relaxation after the coalescence is also intriguing. For instance, the first example given in Figure 8 and Movie S4 (Supporting Information) ended up with a bicrystal, although the second one (Figure 9A and Movie S5, Supporting Information) became a single crystal. Such a difference may derive from some environmental factors, like the orientation between two crystals just before the coalescence, heat, and a large chemical potential that comes from surface tension. Nonetheless, it is obvious that twin crystals are obtained as a result of coalescence rather than during the continuous growth, as expected by many researchers on colloidal nanoparticles.

## ■ CONCLUSION

A new approach for in situ TEM observation of nanoparticle generation was presented using an ionic liquid as a matrix. The

nucleation and growth processes were successfully observed by reducing gold ions through the radiolysis of the ionic liquids. Furthermore, Ostwald ripening and coalescence processes were observed at an atomic resolution in relation to particle–particle interactions. The improved resolution is caused by the nonvolatile nature of ionic liquids, which enables the TEM observation of liquids without a special fluid cell. The observed particle motion was reasonable compared with previous in situ TEM studies using normal solvents. In fact, the order of magnitude lower diffusion coefficient, partly by virtue of the high viscosity of ionic liquids, might actually accentuate the particle–particle interaction. Therefore, the ionic liquids used in this study did not show any anomalous effects on the generation of nanoparticles than those observed in recent in situ TEM studies using conventional solvents. In the manner in which the reactivity against electron beam irradiation was tuned, there is room to design ionic liquids to fit a number of reactions one might wish to investigate. In addition to the study of nanoparticle formation, the present method has immense potential to elucidate various types of chemical reactions that accompany nanoscale morphological changes, such as the initial process of polymerization.

## EXPERIMENTAL SECTION

**Chemicals.** $[C_4mim][Tf_2N]$ (ultrapure grade) and $[N_{3,1,1,1}][Tf_2N]$ (ultrapure grade) were purchased from Kanto Chemical Co., Inc. They were dried at 373 K for 24 h in vacuo before use. Sodium tetrachloroaurate ($NaAuCl_4$) was purchased from Mitsuwa Chemicals Co., Ltd., and used without further purification. Polyvinyl formal (powder) was obtained from Nisshin EM Corporation.

**TEM Sample Preparation.** For TEM observations, a Hitachi H-7650 TEM was used and operated at 100 kV. A gold grid mesh (200 mesh, Nisshin EM Corporation) was covered with a polyvinyl formal membrane, which was prepared by casting on water as a 1,2-dichloroethane solution. About a 10 nm amorphous carbon layer was deposited on top of the membrane to maintain conductivity. Then, an ionic liquid, which was typically a 1:1 (vol) mixture of $[C_4mim]$-$[Tf_2N]$ and $[N_{3,1,1,1}][Tf_2N]$ containing 0.1 M $NaAuCl_4$, was diluted with ethanol in a concentration of 2 vol % and loaded on the above-prepared TEM grid and dried in air. Ionic liquids can be observed for a prolonged period without any evidence of drying. Prior to the continuous electron beam irradiation, the electron beam was irradiated to several points on the TEM grid while measuring current densities at the imaging plate in order to find out an ionic liquid droplet showing a transmittance of ca. 60%.

For high-resolution TEM (HRTEM) observations, a Hitachi H-9000 TEM operated at 300 kV was used. A commercial gold grid with a carbon supporter (Quantifoil, R0.6/1 Holey Carbon TEM Grid Au 200 mesh) was also used. All other conditions for observation were identical to those adopted for low-resolution TEM observations.

## ASSOCIATED CONTENT

**Ⓢ Supporting Information**

Video files and correspondence table for the video files. This material is available free of charge via the Internet at http://pubs.acs.org.

## AUTHOR INFORMATION

**Corresponding Author**
kuwabata@chem.eng.osaka-u.ac.jp

**Notes**

The authors declare no competing financial interest.

## ACKNOWLEDGMENTS

## REFERENCES

(1) Daniel, M. C.; Astruc, D. *Chem. Rev.* **2004**, *104*, 293.
(2) Prasad, B. L. V.; Sorensen, C. M.; Klabunde, K. J. *Chem. Soc. Rev.* **2008**, *37*, 1871.
(3) Hutchings, G. J.; Brust, M.; Schmidbaur, H. *Chem. Soc. Rev.* **2008**, *37*, 1759.
(4) Teranishi, T.; Kiyokawa, I.; Miyake, M. *Adv. Mater.* **1998**, *10*, 596.
(5) Jana, N. R. *Small* **2005**, *1*, 875.
(6) Hussain, I.; Graham, S.; Wang, Z.; Tan, B.; Sherrington, D. C.; Rannard, S. P.; Cooper, A. I.; Brust, M. *J. Am. Chem. Soc.* **2005**, *127*, 16398.
(7) Hiramatsu, H.; Osterloh, F. E. *Chem. Mater.* **2004**, *16*, 2509.
(8) Lamer, V. K.; Dinegar, R. H. *J. Am. Chem. Soc.* **1950**, *72*, 4847.
(9) Overbeek, J. T. G. *Adv. Colloid Interface Sci.* **1982**, *15*, 251.
(10) Privman, V.; Goia, D. V.; Park, J.; Matijević, E. *J. Colloid Interface Sci.* **1999**, *213*, 36.
(11) Voorhees, P. W. *J. Stat. Phys.* **1985**, *38*, 231.
(12) Meli, L.; Green, P. F. *ACS Nano* **2008**, *2*, 1305.
(13) Shields, S. P.; Richards, V. N.; Buhro, W. E. *Chem. Mater.* **2010**, *22*, 3212.
(14) Harada, M.; Kamigaito, Y. *Langmuir* **2012**, *28*, 2415.
(15) Xie, R.; Li, Z.; Peng, X. *J. Am. Chem. Soc.* **2009**, *131*, 15457.
(16) Bullen, C. R.; Mulvaney, P. *Nano Lett.* **2004**, *4*, 2303.
(17) Peng, Z. A.; Peng, X. *J. Am. Chem. Soc.* **2002**, *124*, 3343.
(18) De Jonge, N.; Ross, F. M. *Nat. Nanotechnol.* **2011**, *6*, 695.
(19) Williamson, M. J.; Tromp, R. M.; Vereecken, P. M.; Hull, R.; Ross, F. M. *Nat. Mater.* **2003**, *2*, 532.
(20) Zheng, H.; Smith, R. K.; Jun, Y. W.; Kisielowski, C.; Dahmen, U.; Paul Alivisatos, A. *Science* **2009**, *324*, 1309.
(21) Li, D.; Nielsen, M. H.; Lee, J. R. I.; Frandsen, C.; Banfield, J. F.; De Yoreo, J. J. *Science* **2012**, *336*, 1014.
(22) Yuk, J. M.; Park, J.; Ercius, P.; Kim, K.; Hellebusch, D. J.; Crommie, M. F.; Lee, J. Y.; Zettl, A.; Alivisatos, A. P. *Science* **2012**, *336*, 61.
(23) Liu, X. H.; Liu, Y.; Kushima, A.; Zhang, S.; Zhu, T.; Li, J.; Huang, J. Y. *Adv. Energy Mater.* **2012**, *2*, 722.
(24) Zhong, L.; Liu, X. H.; Wang, G. F.; Mao, S. X.; Huang, J. Y. *Phys. Rev. Lett.* **2011**, *106*, 248302.
(25) Liu, X. H.; Huang, J. Y. *Energy Environ. Sci.* **2011**, *4*, 3844.
(26) Wang, C. M.; Li, X.; Wang, Z.; Xu, W.; Liu, J.; Gao, F.; Kovarik, L.; Zhang, J. G.; Howe, J.; Burton, D. J.; Liu, Z.; Xiao, X.; Thevuthasan, S.; Baer, D. R. *Nano Lett.* **2012**, *12*, 1624.
(27) Gu, M.; Li, Y.; Li, X.; Hu, S.; Zhang, X.; Xu, W.; Thevuthasan, S.; Baer, D. R.; Zhang, J. G.; Liu, J.; Wang, C. *ACS Nano* **2012**, *6*, 8439.
(28) Lee, S.; Oshima, Y.; Hosono, E.; Zhou, H.; Kim, K.; Chang, H. M.; Kanno, R.; Takayanagi, K. *J. Phys. Chem. C* **2013**, *117*, 24236.
(29) Arimoto, S.; Oyamatsu, D.; Torimoto, T.; Kuwabata, S. *ChemPhysChem* **2008**, *9*, 763.
(30) Arimoto, S.; Kageyama, H.; Torimoto, T.; Kuwabata, S. *Electrochem. Commun.* **2008**, *10*, 1901.
(31) Torimoto, T.; Okazaki, K. I.; Kiyama, T.; Hirahara, K.; Tanaka, N.; Kuwabata, S. *Appl. Phys. Lett.* **2006**, *89*, 243117.
(32) Okazaki, K. I.; Kiyama, T.; Hirahara, K.; Tanaka, N.; Kuwabata, S.; Torimoto, T. *Chem. Commun.* **2008**, 691.
(33) Torimoto, T.; Tsuda, T.; Okazaki, K. I.; Kuwabata, S. *Adv. Mater.* **2010**, *22*, 1196.
(34) Kuwabata, S.; Tsuda, T.; Torimoto, T. *J. Phys. Chem. Lett.* **2010**, *1*, 3177.
(35) Lovelock, K. R. J.; Villar-Garcia, I. J.; Maier, F.; Steinrück, H. P.; Licence, P. *Chem. Rev.* **2010**, *110*, 5158.

(36) Wender, H.; Migowski, P.; Feil, A. F.; Teixeira, S. R.; Dupont, J. *Coord. Chem. Rev.* **2013**, *257*, 2468.

(37) Imanishi, A.; Tamura, M.; Kuwabata, S. *Chem. Commun.* **2009**, 1775.

(38) Imanishi, A.; Gonsui, S.; Tsuda, T.; Kuwabata, S.; Fukui, K. I. *Phys. Chem. Chem. Phys.* **2011**, *13*, 14823.

(39) Tsuda, T.; Seino, S.; Kuwabata, S. *Chem. Commun.* **2009**, 6792.

(40) Tsuda, T.; Sakamoto, T.; Nishimura, Y.; Seino, S.; Imanishi, A.; Kuwabata, S. *Chem. Commun.* **2012**, *48*, 1925.

(41) Scheeren, C. W.; Machado, G.; Teixeira, S. R.; Morais, J.; Domingos, J. B.; Dupont, J. *J. Phys. Chem. B* **2006**, *110*, 13011.

(42) Fonseca, G. S.; Machado, G.; Teixeira, S. R.; Fecher, G. H.; Morais, J.; Alves, M. C. M.; Dupont, J. *J. Colloid Interface Sci.* **2006**, *301*, 193.

(43) Reimer, L.; Kohl, H. *Transmission Electron Microscopy: Physics of Image Formation*, 5th ed.; Springer Science+Business Media: New York, 2008.

(44) Jungjohann, K. L.; Evans, J. E.; Aguiar, J. A.; Arslan, I.; Browning, N. D. *Microsc. Microanal.* **2012**, *18*, 621.

(45) Malis, T.; Cheng, S. C.; Egerton, R. F. *J. Electron Microsc. Technol.* **1988**, *8*, 193.

(46) Wishart, J. F. *J. Phys. Chem. Lett.* **2010**, *1*, 3225.

(47) Shkrob, I. A.; Wishart, J. F. *J. Phys. Chem. B* **2009**, *113*, 5582.

(48) Schüth, F.; Bussian, P.; Ågren, P.; Schunk, S.; Lindén, M. *Solid State Sci.* **2001**, *3*, 801.

(49) Erdemir, D.; Lee, A. Y.; Myerson, A. S. *Acc. Chem. Res.* **2009**, *42*, 621.

(50) Oleshko, V. P.; Howe, J. M. In *Advances in Imaging and Electron Physics*; Academic Press: Waltham, MA, 2013; Vol. *179*, p 203.

(51) Zheng, H.; Claridge, S. A.; Minor, A. M.; Alivisatos, A. P.; Dahmen, U. *Nano Lett.* **2009**, *9*, 2460.

(52) Liao, H. G.; Cui, L.; Whitelam, S.; Zheng, H. *Science* **2012**, *336*, 1011.

(53) Atkin, R.; Borisenko, N.; Drüschler, M.; El Abedin, S. Z.; Endres, F.; Hayes, R.; Huber, B.; Roling, B. *Phys. Chem. Chem. Phys.* **2011**, *13*, 6849.

(54) Jeon, Y.; Sung, J.; Bu, W.; Vaknin, D.; Ouchi, Y.; Kim, D. *J. Phys. Chem. C* **2008**, *112*, 19649.

(55) Sloutskin, E.; Ocko, B. M.; Tamam, L.; Kuzmenko, I.; Gog, T.; Deutsch, M. *J. Am. Chem. Soc.* **2005**, *127*, 7796.

(56) Nishi, N.; Yasui, Y.; Uruga, T.; Tanida, H.; Yamada, T.; Nakayama, S. I.; Matsuoka, H.; Kakiuchi, T. *J. Chem. Phys.* **2010**, *132*, 164705.

(57) Fukuda, M.; Terazima, M.; Kimura, Y. *J. Chem. Phys.* **2008**, *128*, 114508.

(58) Makino, W.; Kishikawa, R.; Mizoshiri, M.; Takeda, S.; Yao, M. *J. Chem. Phys.* **2008**, *129*, 104510.

(59) Daguenet, C.; Dyson, P. J.; Krossing, I.; Oleinikova, A.; Slattery, J.; Wakai, C.; Weingärtner, H. *J. Phys. Chem. B* **2006**, *110*, 12682.

(60) Weingärtner, H.; Knocks, A.; Schrader, W.; Kaatze, U. *J. Phys. Chem. A* **2001**, *105*, 8646.

(61) Wang, Z. L.; Mohamed, M. B.; Link, S.; El-Sayed, M. A. *Surf. Sci.* **1999**, *440*, L809.